NANO LETTERS

Letter

pubs.acs.org/NanoLett

Midinfrared Electro-optic Modulation in Few-Layer Black Phosphorus

Ruoming Peng, Kaveh Khaliji, Nathan Youngblood, Roberto Grassi, Tony Low,* and Mo Li*

Department of Electrical and Computer Engineering, University of Minnesota, Minneapolis, Minnesota 55455, United States

Supporting Information

ABSTRACT: Black phosphorus stands out from the family of two-dimensional materials as a semiconductor with a direct, layer-dependent bandgap spanning the visible to mid-infrared (mid-IR) spectral range. It is, therefore, a very promising material for various optoelectronic applications, particularly in the important mid-IR range. While mid-IR technology has been advancing rapidly, both photodetection and electro-optic modulation in the mid-IR rely on narrow-band compound semiconductors, which are difficult and expensive to integrate with the ubiquitous silicon photonics. For mid-IR photodetection, black phosphorus has already been proven to be a viable alternative. Here, we demonstrate electro-optic modulation of mid-IR absorption in few-layer black phosphorus. Our experimental and theoretical results find that, within the doping range obtainable in our samples, the quantum confined Franz−Keldysh effect is the dominant mechanism of electro-optic modulation. A spectroscopic study on samples with varying thicknesses reveals strong layer dependence in the interband transition between specific pairs of sub-bands. Our results show that black phosphorus is a very promising material to realizing efficient mid-IR modulators.

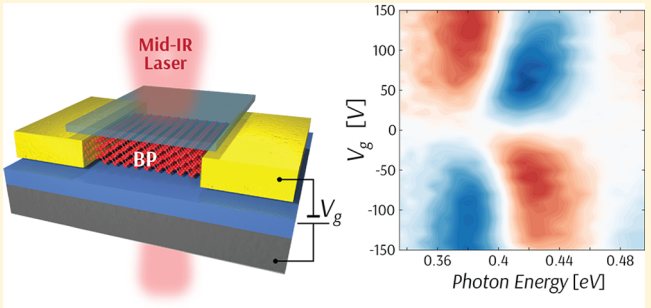

KEYWORDS: *Black phosphorus, midinfrared, quantum confined Franz−Keldysh effect, electro-optic modulation, electro-absorptive modulation, transmission extinction measurement*

Recently, two-dimensional (2D) materials, including graphene, various transition metal dichalcogenides, hexagonal boron nitride, and black phosphorus (BP), have shown great potential in realizing active optoelectronic components in integrated photonics.[1−3] Those include photodetectors,[4−12] optical modulators,[13−15] light emitters, and laser diodes.[16−18] The diverse optical and electronic properties of 2D materials enable optoelectronic functions covering a broad spectral range from the ultraviolet to the visible and from the infrared (IR) to the terahertz. Even more exciting is the possibility of designers' optoelectronic materials at the desired spectral range with a van der Waals heterostructure built from the family of numerous 2D materials.[19] Among all of the 2D materials, black phosphorus has the unique property that its bandgap varies with the number of layers over a very wide range, from around 0.3 eV in the bulk to approximately 1.5−2.0 eV in monolayers (the corresponding optical wavelength range is 0.62−4.1 μm).[20−23] In addition, the hole mobility in BP is as high as 10^4 cm^2/V·s, and the effective masses of electrons and holes are small along the armchair crystal direction.[24] All of these make BP a very promising material for broadband, hyperspectral optoelectronic applications. Indeed, many types of photodetectors based on black phosphorus have been demonstrated, operating in the visible and the near-IR bands.[10−12,25,26] These photodetectors show high responsivity and low dark current—thanks to BP's bandgap, which is a significant advantage over graphene—and a very high response speed.[12] Although the chemical stability of black phosphorus is a concern as it reacts with water and oxygen and quickly degrades when exposed to air,[27,28] BP can be passivated or concealed,[29,30] after which the BP devices can be preserved over a very long time without discernible degradation in device performance. Another challenge faced by BP is the lack of method to grown it in large area, which is under development.[31]

Considering multilayer BP, its bandgap size of around 0.3 eV makes it ideal for optoelectronic applications in the mid-IR range, which has many important applications such as spectroscopic chemical detection and free-space communication.[32,33] It is highly desirable to realize mid-IR systems that are fully integrated, compact, and portable for widespread applications. While mid-IR laser sources have become commercially available[34] and integrated photonic circuits have been developed on the ubiquitous silicon-on-insulator platform,[32,35] mid-IR photodetection still relies on narrowband compound semiconductors such as InAsSb and HgCdTe, which are difficult to be integrated with silicon. As an alternative, BP mid-IR photodetectors have already been demonstrated with promising performance.[25,26] For mid-IR optical modulation, multilayer BP is equally promising.[36] Strong field-effect tuning of its bandgap has been observed in BP, and its infrared optical response has been measured.[37−39]

Received: July 17, 2017
Revised: September 26, 2017
Published: September 27, 2017

ACS Publications © XXXX American Chemical Society

DOI: 10.1021/acs.nanolett.7b03050
Nano Lett. XXXX, XXX, XXX−XXX

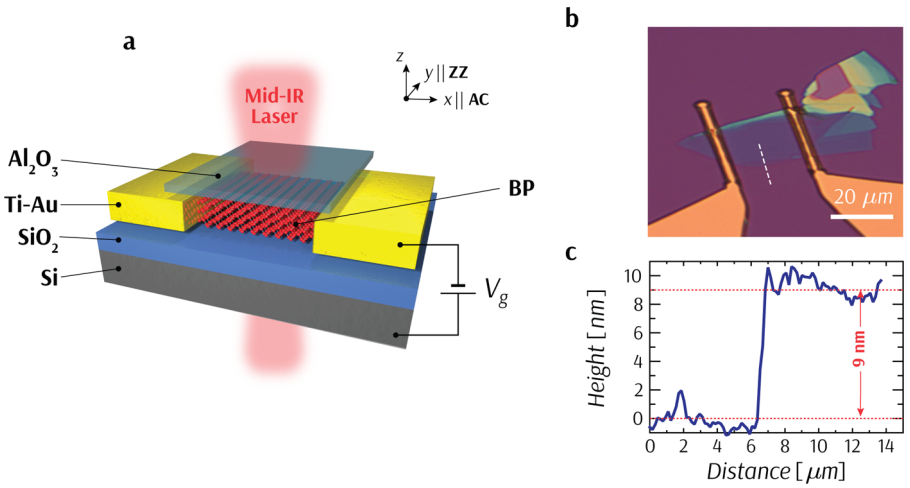

Figure 1. Black phosphorus electro-optic modulator. (a) Schematic illustration of the BP modulator, featuring the normally incident mid-IR laser beam and the lightly p-doped silicon substrate as the back gate. The BP flake is oriented with the arm-chair (AC) crystalline axis along the *x*-axis and the zigzag (ZZ) crystalline axis along the *y*-axis. (b) Optical microscope image of the BP modulator. (c) Height profile (along the dashed line in b) obtained with atomic force microscope shows that the BP thickness is about 9 nm which corresponds to 17 layers.

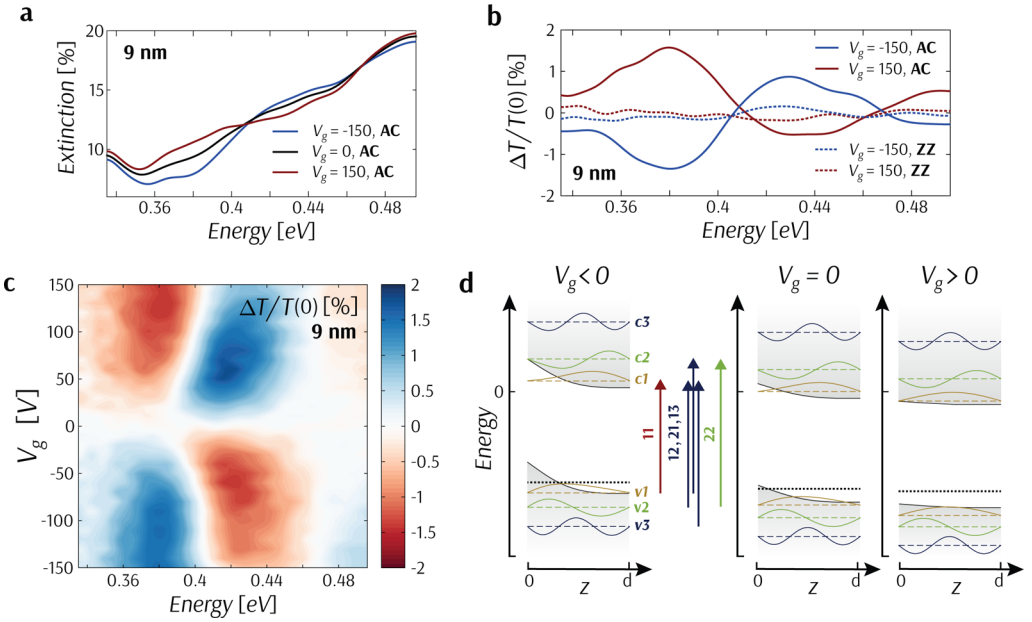

Figure 2. Measurement of mid-IR electro-optic modulation in BP. (a) Measured extinction of the transmitted light for 9 nm BP device at three values of gate voltages V_g = 0, ± 150 V. The incident light is linearly polarized with the electric field parallel to the AC crystalline axis. (b) The modulation level $\Delta T/T(0)$ for 9 nm thick BP at V_g = ±150 V for light polarization along AC (solid lines) and ZZ (dashed lines) crystalline axes. A maximal modulation of about 3% is obtained at a photon energy of 0.38 eV. (c) The modulation level measured as functions of energy and gate bias for 9 nm thick BP. Three characteristic peaks can be observed at E_a = 0.38 eV, E_b = 0.43 eV, and E_c = 0.5 eV. (d) Schematic energy band diagram of BP three sample biases, V_g < 0, V_g = 0, and V_g > 0. The dashed lines in panel d mark the energies of each sub-band. The solid lines depict the wave function in each sub-band. The black dotted line marks the Fermi level. The red/blue/green vertical arrows in panel d show possible transitions that may contribute to the modulation level extrema observed at the characteristic energies of panel c.

Its anisotropic band structure and interband coupling also imbued it with peak-like subband absorption features, which is advantageous for low voltage optical modulation.[40−42] Although graphene has also been used for mid-infrared and terahertz modulation, metamaterial and metasurface structures are utilized to achieve sufficient efficiency.[43−45] Here we report the broadband measurement of electrical modulation of optical absorption in multilayer BP, corroborated with the multiphysics theoretical modeling techniques.[40,41] Our study reveals that the quantum confined Franz−Keldysh effect is the dominant physical mechanism of electro-optic effect in our samples and confirms the viability of using BP to realize an electro-optic modulator in integrated mid-IR photonic systems.[36]

To measure electro-optic modulation in BP, we exfoliated multilayer BP flakes from bulk crystal and used the dry transfer method[46] to transfer them onto a lightly doped silicon substrate with a layer of thermally grown silicon dioxide. To maximize the field at BP/SiO_2 interface for optimal mid-IR absorption in BP, we set the SiO_2 thickness to be 450 nm based on the calculation of the transfer matrix method. Titanium/gold top electrodes were patterned and deposited immediately after the transfer. Finally, 10 nm of alumina was deposited with atomic

DOI: 10.1021/acs.nanolett.7b03050
Nano Lett. XXXX, XXX, XXX−XXX

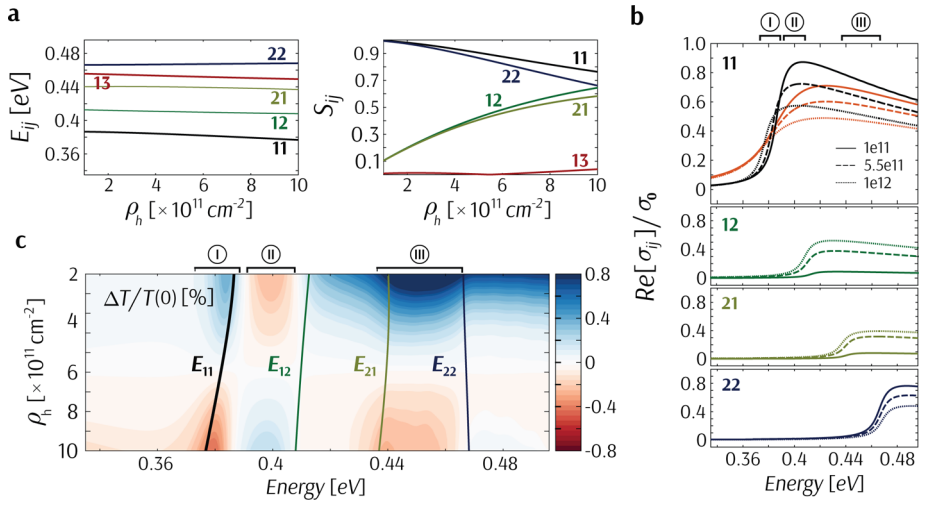

Figure 3. Theoretical calculation of electro-optic modulation for the 9 nm thick BP at room temperature. (a) The transition energy E_{ij} (left panel) and the wave function overlap S_{ij} (right panel) as a function of hole concentration ρ_h. (b) The real part of conductivity σ_{ij} (normalized to $\sigma_0 = e^2/4\hbar$, the universal conductivity of graphene) for various transitions between *ci* and v*j* versus photon energy. (c) Contour plot of the modulation of the transmission as functions of energy and hole concentration. In b and c, broadening is $\eta = 6$ meV, except for the red lines in the top panel b where $\eta = 20$ meV.

layer deposition (ALD) to encapsulate the BP layer and protect it from degradation. A schematic illustration of the device and measurement setup is depicted in Figure 1a. The optical image of a representative device is shown in Figure 1b. The thickness of the BP flake in Figure 1b is determined to be 9 nm with atomic force microscopy (AFM), which corresponds to 17 monolayers. We used a mid-IR optical parametric oscillator (Firefly-IR, M Squared) as the light source outputting nanosecond pulses in the spectral range of 2.5−3.7 μm. The laser beam is focused on the device with a spot size of 20 μm in diameter. The transmitted light is detected with an InAsSb photodetector as the laser output wavelength is scanned to obtain the transmission spectrum of the device. To measure the electro-optic response, we used the Si substrate as the bottom gate while the top electrodes on the BP were grounded. Because silicon has low absorption in the mid-IR range and the substrate is double-side polished, transmission loss due to absorption by the substrate is negligibly small.

Figure 2a shows the measured extinction coefficient, defined as $1 - T(V_g)/T_0$, where T and T_0 denote the powers transmitted through the substrate with and without BP, respectively. The results are shown for three cases where $V_g = 0, \pm 150$ V applied to the back gate, device is under normal illumination, and the incident light is linearly polarized along the armchair (AC) crystalline axis of BP. While the overall transmission shows nonmonotonic energy dependence due to the interference effect in the multilayers of the device, one can observe the gate induced modulation. To reveal the electrostatic control of the transmission, we define the modulation level $[T(V_g) - T(0)]/T(0) = \Delta T/T(0)$, which is computed from the data in Figure 2a and plotted in Figure 2b. $T(0)$ is the transmission when $V_g = 0$ V, which is repeatedly measured and used as the reference point throughout the experiment. In this way, the absorption by the substrate and fluctuation of laser power is nulled out. The result shows clear dependence on the photon energy with (positive and negative) peaks at 0.38 and 0.43 eV, respectively, where modulation level up to 3% is achieved when the gate voltage is switched between ±150 V. Because BP is linearly dichroic due to its anisotropic optical absorption, we also performed similar measurement with light polarization aligned with the zigzag (ZZ) axis. The result displayed as the dashed line in Figure 2b show much weaker modulation level, as expected from theory.[36] The 2D plot in Figure 2c shows systematic measurement results of the modulation level when both photon energy and gate voltage V_g are continuously scanned, which reveals several features worth noting. First, $\Delta T/T(0)$ remains nearly zero, except in the close vicinity of two characteristic photon energies, $E_a = 0.38$ eV and $E_b = 0.43$ eV, where strong modulation can be observed. Second, the sign of $\Delta T/T(0)$ also shows dependence on the polarity of V_g. As V_g changes from negative to positive, at E_a, $\Delta T/T(0)$ changes from positive to negative, while at E_b, the modulation level experiences a negative-to-positive sign flip. In addition, one can also spot in Figure 2c a third characteristic energy with a relatively weak modulation in close proximity of $E_c = 0.5$ eV, where the sign change with gate bias is similar to that observed at E_a.

To gain a qualitative understanding of the results, in Figure 2d, we draw energy band diagrams along the *z*-axis of BP for three situations of gate bias, $V_g < 0$, $V_g = 0$, and $V_g > 0$. We argue that the characteristic energies ($E_{a,b,c}$) in Figure 2c, where the modulation extrema take place, nearly coincide with the transition energies, E_{ij}, between the *i*-th conduction subband (*ci*) and *j*-th valence subband (v*j*). To verify, we compare the experimental values with those obtained with quasi-1D tight binding model:

$$E_{ij} = \Delta_0 - 2(\gamma_c - \gamma_v) + \frac{\pi^2(\gamma_c i^2 - \gamma_v j^2)}{(N+1)^2} \quad (1)$$

where Δ_0 is the monolayer bandgap and N is the number of layers. γ_c and γ_v denote nearest neighbor interlayer coupling for the conduction and valence bands, respectively. We emphasize that expression 1 is valid for flat band condition only. Although flat band condition is not reached in our measurements (to be discussed later), eq 1 can still be used to gain an intuition of the characteristic energies origin. Using the values of the parameters given in ref 41, the transition energies in the energy range of interest for 9 nm BP can be estimated as $E_{11} =$

DOI: 10.1021/acs.nanolett.7b03050
Nano Lett. XXXX, XXX, XXX−XXX

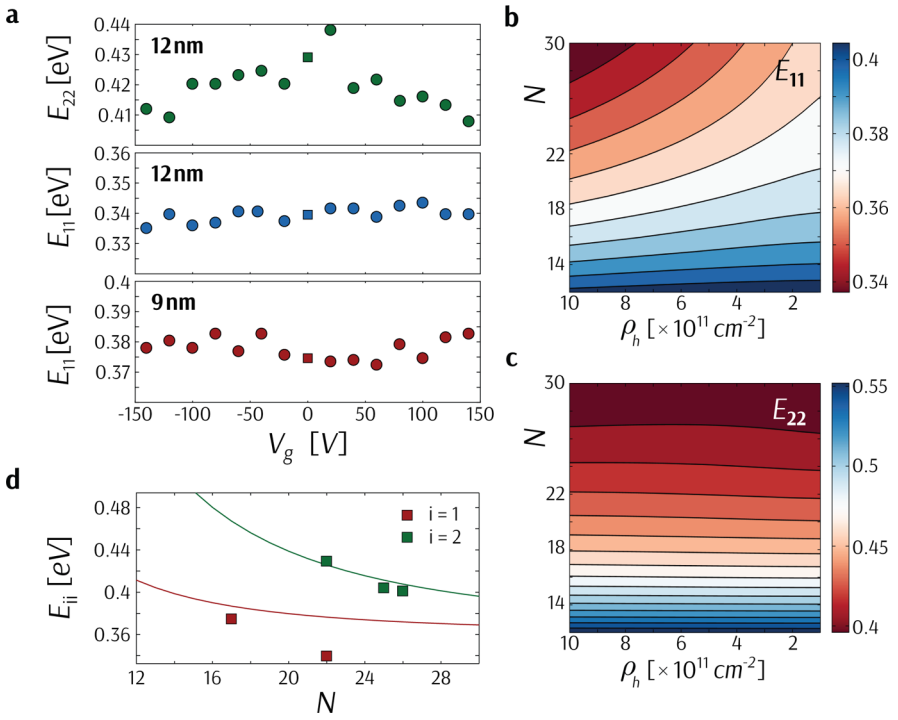

Figure 4. Layer dependence of electro-optic modulation in BP. (a) Gate voltage dependence of E_{11} and E_{22} in 9 and 12 nm thick BP. Squares denote the transition energy at zero gate voltage, obtained via interpolation of the modulation extrema at ±20 V. Contour plots of (b) E_{11} and (c) E_{22} transitions as functions of BP layer number and hole concentration computed via numerical methods. (d) Extracted transition energies at zero gate voltage vs BP layer number. The solid lines represent the data computed via eq 1.

0.39, E_{12} = 0.41, E_{21} = 0.43, E_{13} = 0.44, and E_{22} = 0.47 eV. The comparison suggests that the first and the third modulation exterma in Figure 2c are related to same-index transition energies E_{11} and E_{22}, respectively. The second characteristic energy in Figure 2c, however, seems to originate from hybrid transitions, i.e., between sub-bands with $i \neq j$, though the weighted contribution of each hybrid transition is not clear.

We next examine the sign variation in $\Delta T/T(0)$ and its dependence on bias polarity. A Hall measurement on the sample has shown that the BP is intrinsically p-doped with a hole concentration of $\rho_h = 5.5 \times 10^{11}$ cm^{-2} at zero V_g. Because of the relatively thick oxide layer of the substrate, V_g applied to the back gate is insufficient to tune the BP to the n-doped regime, though the hole concentration ρ_h decreases as V_g changes from negative to positive. For the 11 transition, as V_g becomes more negative, band bending makes the electron and hole wave functions more localized toward the opposite sides of the BP, thereby reducing the conduction-valence overlap and its corresponding oscillator strength, as illustrated in Figure 2d. This leads to a decrease in the absorption at the corresponding photon energy and renders the transmission at negative V_g to be larger than $T(0)$, hence the positive $\Delta T/T(0)$ signs. Conversely, the transmission at positive V_g is lower than $T(0)$, thus the negative $\Delta T/T(0)$ sign. For the 12 transition, however, the wave function overlap increases with the hole concentration. The latter renders a reverse V_g dependence for 12 relative to 11 and, therefore, justifies the opposite signs in $\Delta T/T(0)$ at E_a and E_b of Figure 2c. Similar behavior can also be anticipated for 21 or 13. We emphasize that the observed sign change of the modulation level at E_b due to the hybrid transitions in Figure 2c suggests that the BP cannot be in the flat-band condition when V_g is zero because the hybrid transitions are forbidden under the flat band condition. Instead, the trapped charges at the BP/SiO_2 interface may cause the intrinsic doping to be distributed nonuniformly among the sample layers (see middle panel in Figure 2d) and cause band bending.

To verify the qualitative picture, we resort to multiphysics numerical techniques to solve for the transmission spectra of the geometry shown in Figure 1a. The full account of the models employed are described in Supporting Information, and the results are summarized in Figure 3. The calculated transition energy E_{ij} and wave function overlap S_{ij} at versus hole density ρ_h are illustrated in Figure 3a. As shown, in the relevant range of ρ_h, only the transitions 11, 12, 21, 22, and 13 lie in the energy range of interest. Among those, 13 has near-zero overlap and therefore does not contribute to BP's absorption. For those transitions that contribute, the overlap decreases with ρ_h for 11 and 22 transitions, while it increases for 12 and 21 transitions. Furthermore, the transition energy E_{11} decreases with ρ_h, while the rest are almost not affected by it. The observed trends, namely, the reduction of the optical gap and the localization of the conduction and valence band wave functions along the opposite sides of the BP, are indeed consistent with the Franz−Keldysh effect in quantum wells under the perpendicular static electric field.[47]

The real parts of the conductivity due to various subband transitions at three ρ_h values are shown in Figure 3b. For the 11 transition, one can identify a red-shift in the absorption edge with increasing ρ_h, which is also observable for E_{11} in Figure 3a. Furthermore, the consistent change in both conductivity peaks and wave function overlapping with ρ_h suggests a direct link between the two quantities. To compare with the experimental results, we calculate the modulation level $\Delta T/T(0)$ as a function of ρ_h and photon energy as shown in Figure 3c, where $T(0)$ is the optical transmission when $\rho_h = 5.5 \times 10^{11}$ cm^{-2}.

DOI: 10.1021/acs.nanolett.7b03050
Nano Lett. XXXX, XXX, XXX−XXX

From the figure, one can identify three energy intervals, specified as I, II, and II, where transmission modulation changes sign with ρ_h. Comparing the results in Figure 3b and c, it is evident that interval I and II are both related to 11 transition. More precisely, interval I originates from the shift in the absorption edge, while II is due to the change in wave function overlap. For interval III, however, all four transitions specified in Figure 3b contribute and the competition between 11 and 22 transitions on the one hand, and 12 and 21 on the other, determines how the modulation changes sign with ρ_h. Nonetheless, in general, a negative-to-positive sign flip in $\Delta T/T(0)$ with increasing ρ_h can mainly be attributed to same-index transitions. A positive-to-negative sign change of $\Delta T/T(0)$, however, has a more complex origin as it can be caused by both the energy shift of same-index transitions and the increase in wave function overlap of the hybrid transitions. The two mechanisms can be discriminated, however, via inspecting the energy separation of the immediate next sign flip. To elaborate, if the positive-to-negative sign change in $\Delta T/T(0)$ were due to the shift in E_{ii} transition, an opposite sign flip in modulation level should follow at immediate energies. This is due to the fact that for same-index transitions, the red shift in the absorption edge is always followed by a decrease in the wave function overlap (see, e.g., the top panel in Figure 3b).

Armed with this general conclusion inferred from Figure 3, we now re-examine the experimental results in Figure 2c. Emphasizing again that ρ_h in this sample increases with positive-to-negative V_g change, the negative-to-positive sign flip in $\Delta T/T(0)$ at energies E_a and E_c, can be unambiguously attributed to same-index transitions. For the second characteristic energy, E_b, the positive-to-negative sign change in $\Delta T/T(0)$ with ρ_h along with the fact that it is well-separated from E_c (i.e., the modulation sign change at E_b is not followed by an immediate opposite sign flip), certify that hybrid transitions are indeed responsible. As a final remark, we discuss why the bias induced redshift in 11 transition and its corresponding modulation sign change (i.e., interval I in Figure 3c) does not appear in the experimental result. As mentioned previously, the edge shift induced sign change should happen in energies just before a sign flip induced by the wave function overlap. Since the accessible energy range in our measurements is limited, and the overlap induced sign flip is broadened in the energy range of 0.34−0.4 eV, we might have missed the edge-shift induced sign flip. Alternately, one can argue that the appearance of the edge shift induced sign change is highly sensitive to the loss in BP, which is modeled with a phenomenological loss term, denoted as η in the Kubo formula. As shown in Figure 3b, top panel, with increasing η, the 11 conductivity peak becomes more broadened, and the absorption edge shift is no longer apparent.

We next focus on how bias-induced modulation of transmission spectra depends on BP thickness. In Figure 4a, we report the same-index transition energies E_{ii} extracted from the contour plots of modulation level by tracing the modulation extrema. As shown, E_{11} in 9 nm thick device remains nearly unchanged with gate bias. For a different device with 12 nm thick BP, however, we observe E_{11} decreases monotonically for a positive-to-negative change of V_g, whereas E_{22} exhibits a maximum at V_g = 20 V. These observations are indeed consistent with the results obtained via our numerical calculation. In Figure 4b, E_{11} shows a much stronger red shift with increasing ρ_h in thicker BP than in thinner BP. For E_{22}, it develops a maximum with ρ_h as the number of layers increases. We should mention that, for hybrid transitions, it is not possible to pin down the V_g modulation of individual hybrid transitions as they overlap to form one modulation extrema (e.g., E_b in Figure 2c).

In Figure 4d, the same-index transition energies at zero V_g are shown as a function of the number of layers N. The strong decrease in transition energies with N is evident. Also shown in the figure are the transition energies (solid lines) obtained from eq 1. While the extracted E_{22} at zero V_g follows eq 1, for the 11 transition, eq 1 cannot properly recover the fast descending trend observed in the measurements. These can be explained by referring to Figure 2d showing the presence of band bending at zero V_g in our samples. Compared with the 22 transition, the 11 transition is more susceptible to this band bending and therefore does not follow eq 1, which describes only the flat band condition. The deviation further increases in thicker samples as the first conduction (valence) subbands move toward lower (higher) energies, thereby sensing the band bending more effectively.

In conclusion, we have demonstrated electro-optic modulation of multilayer BP in the mid-IR range, which is dominated by the quantum confined Franz−Keldysh effect. Peaks of modulation level at different photon energies are related to contributions from optical transitions between different subbands, which show strong layer and gate voltage dependence. We expect the performance of a BP electro-optic modulator would be improved significantly when a high-k dielectric material such as HfO_2 is used as the gate oxide. When integrated with a waveguide, the light will propagate along the plane of the BP with a much longer interaction length. A recent study, using parameters consistent with our experimental results (see SI), predicts that a modulation level of 0.05 dB/μm is attainable in a waveguide integrated BP modulator. This suggests that a 5 dB modulation depth can be achieved with a 100 μm device.[36] Such an electro-absorptive modulation utilizing the interband transition in BP as a narrowband 2D semiconductor should be much more efficient than using the carrier plasma dispersion effect in silicon.[48] The performance can be further improved with novel device design and integration, as those have been proposed and implemented for graphene-based modulators working in the near-infrared regime.[13−15,49] The above results and prospects indicate that BP is a very promising material in mid-IR optoelectronic devices for a wide range of applications.

■ ASSOCIATED CONTENT

Supporting Information

The Supporting Information is available free of charge on the ACS Publications website at DOI: 10.1021/acs.nanolett.7b03050.

Details of theoretical and numerical methods; measurement setup; fabrication methods; electrical characterization; results from more devices with different black phosphorus thicknesses (PDF)

■ AUTHOR INFORMATION

Corresponding Authors

*E-mail: tlow@umn.edu.

*E-mail: moli@umn.edu.

ORCID

Nathan Youngblood: 0000-0003-2552-9376

Mo Li: 0000-0002-5500-0900

DOI: 10.1021/acs.nanolett.7b03050
Nano Lett. XXXX, XXX, XXX−XXX

Notes

The authors declare no competing financial interest.

■ ACKNOWLEDGMENTS

This work was supported by the Air Force Office of Scientific Research (award no. FA9550-14-1-0277; R.P., N.Y., M.L.) and the National Science Foundation (award no. ECCS-1351002 for R.P., N.Y., M.L.; University of Minnesota MRSEC under award no. DMR-1420013 for K.K.). Device fabrication was carried out at the University of Minnesota Nanofabrication Center, which receives partial support from the NSF through the National Nanotechnology Coordinated Infrastructure (NNCI) program. The authors also used resources at the Characterization Facility, which is a member of the NSF-funded Materials Research Facilities Network via the NSF MRSEC program.

■ REFERENCES

(1) Kim, K.; Choi, J.-Y.; Kim, T.; Cho, S.-H.; Chung, H.-J. *Nature* **2011**, *479* (7373), 338−44.
(2) Novoselov, K. S.; Fal' ko, V. I.; Colombo, L.; Gellert, P. R.; Schwab, M. G.; Kim, K. *Nature* **2012**, *490* (7419), 192−200.
(3) Xia, F.; Wang, H.; Xiao, D.; Dubey, M.; Ramasubramaniam, A. *Nat. Photonics* **2014**, *8* (12), 899−907.
(4) Xia, F.; Mueller, T.; Lin, Y. M.; Valdes-Garcia, A.; Avouris, P. *Nat. Nanotechnol.* **2009**, *4* (12), 839−43.
(5) Mueller, T.; Xia, F.; Avouris, P. *Nat. Photonics* **2010**, *4*, 297−301.
(6) Lopez-Sanchez, O.; Lembke, D.; Kayci, M.; Radenovic, A.; Kis, A. *Nat. Nanotechnol.* **2013**, *8* (7), 497−501.
(7) Gan, X.; Shiue, R.-J.; Gao, Y.; Meric, I.; Heinz, T. F.; Shepard, K.; Hone, J.; Assefa, S.; Englund, D. *Nat. Photonics* **2013**, *7* (11), 883−887.
(8) Wang, X.; Cheng, Z.; Xu, K.; Tsang, H. K.; Xu, J.-B. *Nat. Photonics* **2013**, *7* (11), 888−891.
(9) Pospischil, A.; Humer, M.; Furchi, M. M.; Bachmann, D.; Guider, R.; Fromherz, T.; Mueller, T. *Nat. Photonics* **2013**, *7* (11), 892−896.
(10) Engel, M.; Steiner, M.; Avouris, P. *Nano Lett.* **2014**, *14* (11), 6414−6417.
(11) Yuan, H.; Liu, X.; Afshinmanesh, F.; Li, W.; Xu, G.; Sun, J.; Lian, B.; Curto, A. G.; Ye, G.; Hikita, Y.; Shen, Z.; Zhang, S.-C.; Chen, X.; Brongersma, M.; Hwang, H. Y.; Cui, Y. *Nat. Nanotechnol.* **2015**, *10* (8), 707−713.
(12) Youngblood, N.; Chen, C.; Koester, S. J.; Li, M. *Nat. Photonics* **2015**, *9* (4), 247−252.
(13) Liu, M.; Yin, X.; Ulin-Avila, E.; Geng, B.; Zentgraf, T.; Ju, L.; Wang, F.; Zhang, X. *Nature* **2011**, *474* (7349), 64−7.
(14) Youngblood, N.; Anugrah, Y.; Ma, R.; Koester, S. J.; Li, M. *Nano Lett.* **2014**, *14* (5), 2741−2746.
(15) Phare, C. T.; Lee, Y.-H. D.; Cardenas, J.; Lipson, M. *Nat. Photonics* **2015**, *9* (8), 511−514.
(16) Wu, S.; Buckley, S.; Schaibley, J. R.; Feng, L.; Yan, J.; Mandrus, D. G.; Hatami, F.; Yao, W.; Vuckovic, J.; Majumdar, A.; Xu, X. *Nature* **2015**, *520* (7545), 69−72.
(17) Liu, C. H.; Clark, G.; Fryett, T.; Wu, S.; Zheng, J.; Hatami, F.; Xu, X.; Majumdar, A. *Nano Lett.* **2017**, *17* (1), 200−205.
(18) Palacios-Berraquero, C.; Barbone, M.; Kara, D. M.; Chen, X.; Goykhman, I.; Yoon, D.; Ott, A. K.; Beitner, J.; Watanabe, K.; Taniguchi, T.; Ferrari, A. C.; Atature, M. *Nat. Commun.* **2016**, *7*, 12978.
(19) Geim, A. K.; Grigorieva, I. V. *Nature* **2013**, *499* (7459), 419−425.
(20) Keyes, R. W. *Phys. Rev.* **1953**, *92* (3), 580−584.
(21) Das, S.; Zhang, W.; Demarteau, M.; Hoffmann, A.; Dubey, M.; Roelofs, A. *Nano Lett.* **2014**, *14* (10), 5733−5739.
(22) Li, L.; Yu, Y.; Ye, G. J.; Ge, Q.; Ou, X.; Wu, H.; Feng, D.; Chen, X. H.; Zhang, Y. *Nat. Nanotechnol.* **2014**, *9* (5), 372−377.
(23) Ling, X.; Wang, H.; Huang, S.; Xia, F.; Dresselhaus, M. S. *Proc. Natl. Acad. Sci. U. S. A.* **2015**, *112* (15), 4523−4530.
(24) Qiao, J.; Kong, X.; Hu, Z. X.; Yang, F.; Ji, W. *Nat. Commun.* **2014**, *5*, 4475.
(25) Guo, Q.; Pospischil, A.; Bhuiyan, M.; Jiang, H.; Tian, H.; Farmer, D.; Deng, B.; Li, C.; Han, S.-J.; Wang, H.; Xia, Q.; Ma, T.-P.; Mueller, T.; Xia, F. *Nano Lett.* **2016**, *16* (7), 4648−4655.
(26) Xu, M.; Gu, Y. Q.; Peng, R. M.; Youngblood, N.; Li, M. *Appl. Phys. B: Lasers Opt.* **2017**, *123* (4), 130.
(27) Huang, Y.; Qiao, J.; He, K.; Bliznakov, S.; Sutter, E.; Chen, X.; Luo, D.; Meng, F.; Su, D.; Decker, J. *Chem. Mater.* **2016**, *28* (22), 8330−8339.
(28) Hu, Z.; Li, Q.; Lei, B.; Zhou, Q.; Xiang, D.; Lyu, Z.; Hu, F.; Wang, J.; Ren, Y.; Guo, R.; Goki, E.; Wang, L.; Han, C.; Wang, J.; Chen, W. *Angew. Chem., Int. Ed.* **2017**, *56* (31), 9131−9135.
(29) Artel, V.; Guo, Q.; Cohen, H.; Gasper, R.; Ramasubramaniam, A.; Xia, F.; Naveh, D. *npj 2D Materials and Applications* **2017**, *1* (1), 6.
(30) Wood, J. D.; Wells, S. A.; Jariwala, D.; Chen, K.-S.; Cho, E.; Sangwan, V. K.; Liu, X.; Lauhon, L. J.; Marks, T. J.; Hersam, M. C. *Nano Lett.* **2014**, *14* (12), 6964−6970.
(31) Smith, J. B.; Hagaman, D.; Ji, H.-F. *Nanotechnology* **2016**, *27* (21), 215602.
(32) Soref, R. *Nat. Photonics* **2010**, *4* (8), 495−497.
(33) Stanley, R. *Nat. Photonics* **2012**, *6* (7), 409−411.
(34) Yao, Y.; Hoffman, A. J.; Gmachl, C. F. *Nat. Photonics* **2012**, *6* (7), 432−439.
(35) Miller, S. A.; Yu, M.; Ji, X.; Griffith, A. G.; Cardenas, J.; Gaeta, A. L.; Lipson, M. *Optica* **2017**, *4* (7), 707−712.
(36) Lin, C.; Grassi, R.; Low, T.; Helmy, A. S. *Nano Lett.* **2016**, *16* (3), 1683−1689.
(37) Kim, J.; Baik, S. S.; Ryu, S. H.; Sohn, Y.; Park, S.; Park, B.-G.; Denlinger, J.; Yi, Y.; Choi, H. J.; Kim, K. S. *Science* **2015**, *349* (6249), 723−726.
(38) Whitney, W. S.; Sherrott, M. C.; Jariwala, D.; Lin, W. H.; Bechtel, H. A.; Rossman, G. R.; Atwater, H. A. *Nano Lett.* **2017**, *17* (1), 78−84.
(39) Deng, B.; Tran, V.; Xie, Y.; Jiang, H.; Li, C.; Guo, Q.; Wang, X.; Tian, H.; Koester, S. J.; Wang, H.; Cha, J. J.; Xia, Q.; Yang, L.; Xia, F. *Nat. Commun.* **2017**, *8*, 14474.
(40) Low, T.; Rodin, A.; Carvalho, A.; Jiang, Y.; Wang, H.; Xia, F.; Neto, A. C. *Phys. Rev. B: Condens. Matter Mater. Phys.* **2014**, *90* (7), 075434.
(41) Zhang, G.; Huang, S.; Chaves, A.; Song, C.; Özçelik, V. O.; Low, T.; Yan, H. *Nat. Commun.* **2017**, *8*, 14071.
(42) Li, L.; Kim, J.; Jin, C.; Ye, G. J.; Qiu, D. Y.; da Jornada, F. H.; Shi, Z.; Chen, L.; Zhang, Z.; Yang, F. *Nat. Nanotechnol.* **2016**, *12* (1), 21−25.
(43) Yao, Y.; Shankar, R.; Kats, M. A.; Song, Y.; Kong, J.; Loncar, M.; Capasso, F. *Nano Lett.* **2014**, *14* (11), 6526−6532.
(44) Ju, L.; Geng, B.; Horng, J.; Girit, C.; Martin, M.; Hao, Z.; Bechtel, H. A.; Liang, X.; Zettl, A.; Shen, Y. R. *Nat. Nanotechnol.* **2011**, *6* (10), 630−634.
(45) Sensale-Rodriguez, B.; Yan, R.; Kelly, M. M.; Fang, T.; Tahy, K.; Hwang, W. S.; Jena, D.; Liu, L.; Xing, H. G. *Nat. Commun.* **2012**, *3*, 780.
(46) Dean, C. R.; Young, A. F.; Meric, I.; Lee, C.; Wang, L.; Sorgenfrei, S.; Watanabe, K.; Taniguchi, T.; Kim, P.; Shepard, K. L.; Hone, J. *Nat. Nanotechnol.* **2010**, *5* (10), 722−726.
(47) Miller, D.; Chemla, D.; Schmitt-Rink, S. *Phys. Rev. B: Condens. Matter Mater. Phys.* **1986**, *33* (10), 6976.
(48) Nedeljkovic, M.; Soref, R.; Mashanovich, G. Z. *IEEE Photonics J.* **2011**, *3* (6), 1171−1180.
(49) Koester, S. J.; Li, M. *Appl. Phys. Lett.* **2012**, *100*, 171107.

DOI: 10.1021/acs.nanolett.7b03050
Nano Lett. XXXX, XXX, XXX−XXX